Nano Research

Open Access

Research Article

Optimal inter-site distance in Cu single-atom catalysts for efficient peroxymonosulfate activation and ciprofloxacin degradation

Panlekha Manpetch[1,2], Yaomeng Yang[1,2], Kaixin Zhou[1,2], Rongrong Xie[1,2], Weiguo Song[1,2] ✉, and Changyan Cao[1,2] ✉

[1] *Beijing National Laboratory for Molecular Sciences, CAS Research/Education Center for Excellence in Molecular Sciences, CAS Key Laboratory of Molecular Nanostructure and Nanotechnology, Institute of Chemistry, Chinese Academy of Sciences, Beijing 100190, China*
[2] *University of Chinese Academy of Sciences, Beijing 100190, China*

Cite this article: *Nano Research*, **2026**, *19*, 94908537. https://doi.org/10.26599/NR.2026.94908537

ABSTRACT: Ciprofloxacin is a widely used antibiotic that persists in aquatic environments, posing environmental risks. Peroxymonosulfate (PMS)-based advanced oxidation processes are promising for ciprofloxacin (CIP) degradation due to their strong oxidative capability. In this work, high-loading Cu single-atom catalysts were synthesized via polycondensation followed by pyrolysis, achieving Cu loadings up to 5.9 at.% with exclusive atomic dispersion confirmed by X-ray diffraction (XRD), field emission scanning electron microscopy (FE-SEM), transmission electron microscopy (TEM), high-angle annular dark-field scanning transmission electron microscopy (HAADF-STEM), and X-ray photoelectron spectroscopy (XPS). By tuning Cu atomic density, the inter-site distance (d_{site}) was systematically regulated from 1.62 to 0.49 nm, and its effect on PMS activation was investigated. The catalyst with the shortest d_{site} (0.49 nm) exhibited superior catalytic performance, achieving complete CIP degradation within 30 min with a kinetic rate constant of 0.3242 min^{-1}. Response surface methodology revealed that the reaction time, catalyst dosage, and PMS concentration significantly influenced degradation efficiency. Although d_{site} alone was not statistically significant (p = 0.162), its interaction with PMS concentration was highly significant (p = 0.001), indicating a synergistic role of the spatial Cu arrangement. Mechanistic studies combining quenching experiments, electronic paramagnetic resonance (EPR) spectroscopy, potassium iodide (KI)-based PMS consumption analysis, and solvent isotope effects demonstrate a dual-pathway PMS activation mechanism dominated by a surface-confined non-radical singlet oxygen ($^1O_2$) pathway, accompanied by auxiliary radical pathways. These results highlight the importance of inter-site distance engineering for designing efficient single-atom catalysts for advanced water treatment.

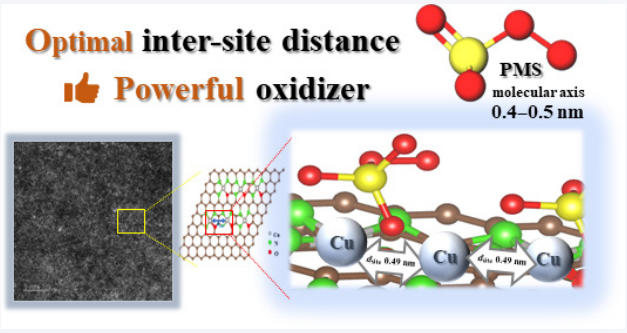

KEYWORDS: advanced oxidation processes, peroxymonosulfate, ciprofloxacin, single-atom catalyst (SAC), inter-site distance (d_{site})

1 Introduction

The widespread use of antibiotics in both human and veterinary medicine has led to their persistent presence in aquatic environments, posing significant ecological and public health risks [1–4]. Ciprofloxacin (CIP), a fluoroquinolone antibiotic, is of particular concern because of its extensive use during the COVID-19 pandemic, as it was reported to inhibit the entry of SARS-CoV-2 into host cells [5]. CIP is resistant to biodegradation and is poorly removed during conventional wastewater treatment processes [1, 6]. Wastewater-based epidemiology monitoring across urban treatment plants in China revealed the presence of quinolones, with CIP detected in approximately 56.4% of the collected samples [6]. Moreover, CIP promotes the development of antibiotic-resistant bacteria [1, 2, 7]. A major challenge in CIP biodegradation is the slow and often incomplete process; even with specialized bacterial strains, degradation can take 5–10 days [8, 9]. Therefore, the removal of CIP from wastewater is crucial to mitigate its environmental impact and prevent the spread of antibiotic-resistant bacteria.

Traditional wastewater treatment methods are often insufficient for degrading these persistent organic pollutants [9], therefore,

Received: November 7, 2025
Accepted: February 3, 2026

✉Address correspondence to Weiguo Song, wsong@iccas.ac.cn; Changyan Cao, cycao@iccas.ac.cn

advanced oxidation processes (AOPs) are required, such as photocatalysis, ozone, Fenton reaction, and electrochemical oxidation, which can efficiently break down these contaminants [3, 4, 7, 9–13]. However, these methods have limitations, including dependence on specific conditions, energy inefficiency, and the generation of secondary pollutants. For instance, photocatalysis relies heavily on light availability and catalyst efficiency, often requiring ultraviolet (UV) or visible light [10, 11], which limits its effectiveness under varying environmental conditions. Ozone treatment is highly pH-dependent and can produce toxic byproducts such as bromate in the presence of bromide ions [11], while the Fenton reaction is optimal only at acidic pH levels of 2–4 [12]. Electrochemical oxidation demands high energy input and specialized equipment, and it can produce toxic chlorinated byproducts in the presence of chloride ions. In contrast, peroxymonosulfate-based AOPs (PMS-AOPs) offer a more effective and sustainable solution. PMS-AOPs generate highly reactive oxygen species (ROS), such as sulfate radicals ($SO_4^{\cdot-}$) and hydroxyl radicals (·OH), which exhibit higher oxidation potentials, longer half-lives, and greater selectivity in breaking down complex organic pollutants [3, 7, 14–19]. Unlike other methods, PMS-AOPs operate effectively under a wider range of environmental conditions, do not produce significant sludge or secondary pollutants, and are also energy-efficient [20]. The non-radical pathways, particularly involving singlet oxygen ($^1O_2$), further enhance the effectiveness and sustainability of PMS-AOPs. $^1O_2$ is highly selective toward electron-rich organic pollutants, such as pharmaceuticals, dyes, and phenolic compounds, enabling targeted degradation without oxidation of other components [21–23]. Additionally, non-radical PMS-AOPs are energy efficient and scalable. As demonstrated by Lu et al. [23], single-atom catalysts (SACs) with saturated Cu-N_4 sites exhibited high catalytic performance and selectivity for the pollutant degradation in complex wastewater. The study showed that the catalyst could activate PMS through dual non-radical pathways, primarily involving $^1O_2$ and electron transfer processes, resulting in efficient degradation of pollutants like bisphenol A with minimal energy consumption. By combining the strengths of radical and non-radical pathways, PMS-AOPs offer a versatile and robust solution for degrading persistent organic pollutants, disinfecting water, and treating industrial effluents [22–25].

The generation of radical and non-radical species during PMS activation depends critically on the catalyst employed [26]. Among the various catalysts, SACs have demonstrated remarkable advantages over conventional catalysts [16, 17, 27], including high atom utilization, unique electronic and geometric properties, enhanced stability, improved selectivity, lower energy requirements, and greater versatility [28, 29]. These attributes make SACs highly effective, in part because their optimized electronic structures enable efficient electron transfer and lower the energy barrier for ROS generation, thereby significantly enhancing the catalytic performance and stability [30–32]. The effectiveness of SACs in catalytic reactions is also influenced by the inter-site distance (d_{site}) between active sites, particularly in high-loading SACs [28, 30, 33, 34]. Specifically, the d_{site} between isolated metal atoms in high-loading SACs can significantly influence the adsorption configuration and activation pathways of reactant molecules [33–35], thereby affecting the catalytic performance. Previous studies have shown that the metal–metal distances in the range of 0.4–0.6 nm can promote the cooperative activation in dual-site catalytic systems, including Co–Co for PMS activation [35] and Fe–Fe for O_2 reduction [33]. These studies emphasize that closely positioned atomic sites can engage in synergistic interactions that are inaccessible to isolated single sites. In contrast to these systems, Cu-based SACs have rarely been examined with respect to controlled variations in inter-site distance.

In this study, we explored densely populated Cu SACs, with Cu loading up to 5.9 at.% (21.2 wt.%) for PMS activation in CIP degradation. By systematically varying the atomic loading of Cu, the d_{site} of Cu was tuned from 1.62 to 0.49 nm, allowing the investigation of the d_{site} effect on the catalytic performance. The influence of reaction parameters on the degradation of CIP was further evaluated using response surface methodology (RSM) with a central composite design. The results reveal a clear enhancement in PMS activation efficiency at shorter d_{site} values. In particular, the catalyst with d_{site} of 0.49 nm achieves complete CIP degradation within 30 min through a combination of radical and non-radical pathways. These findings demonstrate that d_{site} plays a critical role in governing PMS activation efficiency, providing a foundation for the rational design of highly efficient single-atom catalysts for environmental remediation.

2 Results and discussion

2.1 Morphological and structural analysis

Figure 1(a) illustrates the two-step synthesis of high-loading Cu SACs, comprising polycondensation followed by pyrolysis. The initial step involves the formation of nanosheets and the anchoring of copper ions. These nanosheets are produced through the spontaneous polymerization of N-rich chemicals, including melamine, cyanuric acid, L-alanine, and phytic acid. The interactions among these molecules establish a robust heteroatom framework, composed of nitrogen and oxygen, within the polymer matrix. Simultaneously, copper ions are anchored within this matrix. Upon pyrolysis at 700 °C under an argon atmosphere, Cu SACs with an N/O-coordination structure are obtained. Due to the precursor's large quantities sites for metal ion anchoring, the high-loading Cu SACs are achieved. In this study, atomic percentage (at.%) is used to define the loading of SACs rather than weight percentage (wt.%), as the at.% provides a more accurate representation of the number of active sites in SACs [36]. As shown in Table 1, the Cu loading in the *x*Cu-NOC samples spanned a range from 0.3 at.% to 5.9 at.%, corresponding to 1.2 wt.% to 21.2 wt.%. The samples were denoted as 0.3Cu-NOC, 2.0Cu-NOC, 3.9Cu-NOC, and 5.9Cu-NOC, respectively.

The XRD patterns shown in Fig. 1(b) for the NOC and *x*Cu-NOC samples exhibit a broad peak at 2θ = 20°–30°, which corresponds to the (002) plane of graphitic carbon. This indicates the presence of a graphitic structure in the N-doped carbon support. No characteristic peaks related to Cu metal or metal oxides across *x*Cu-NOC samples are observed, indicating that the Cu atoms are atomically dispersed and do not form nanoparticles or clusters. Supported by the results from SEM and TEM images (Figs. 1(c) and 1(d), and Figs. S1 and S2 in the Electronic Supplementary Material (ESM)), the surface of NOC and *x*Cu-NOC samples exhibit a lamellar thin-layer nanosheet structure with slight wrinkles, and no nanoparticles or clusters are observed on *x*Cu-NOC.

The atomic dispersion of Cu was directly visualized using

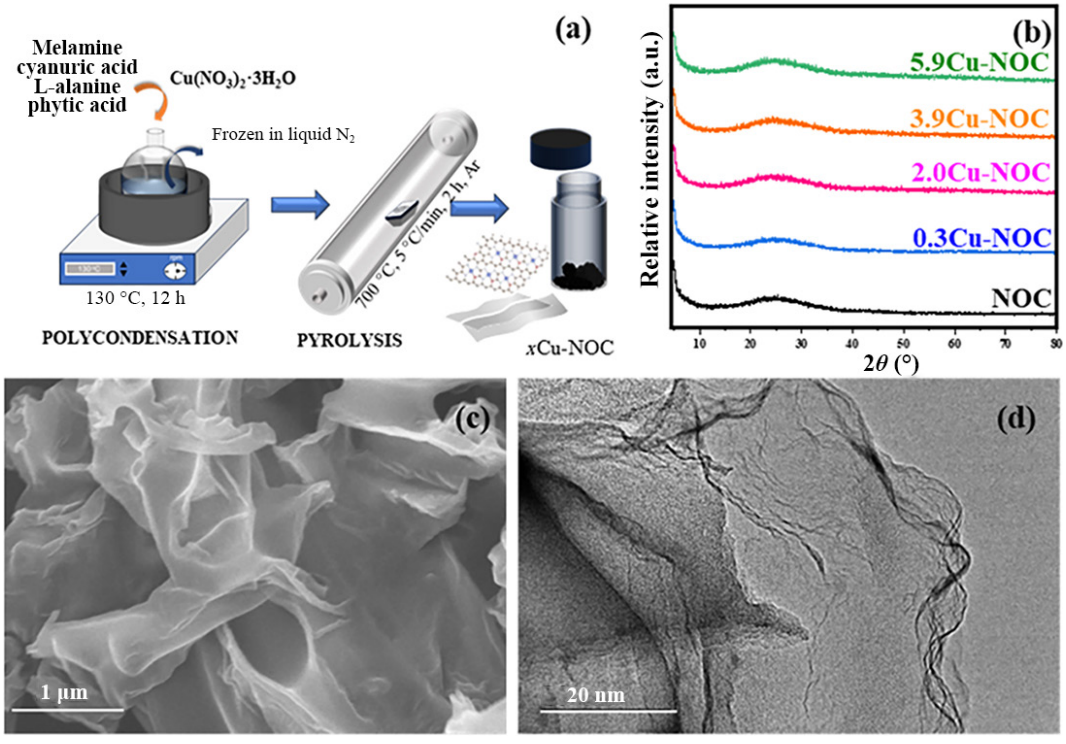

Figure 1 (a) Schematic illustration of the synthesis method for Cu SACs. (b) XRD patterns of Cu-NOC with different Cu atomic percentages. (c) Field emission scanning electron microscopy (FE-SEM) and (d) high resolution TEM (HR-TEM) images of 5.9Cu-NOC, demonstrating the catalyst's morphology.

Table 1 Analysis of the weight and atomic percent content and d_{site} of Cu in Cu SACs

Samples	Weight content (%)	Atomic content (%)	d_{site} Cu_1–Cu_1 (nm)
0.3Cu-NOC	1.2	0.3	1.62 ± 0.10
2.0Cu-NOC	8.0	2.0	0.68 ± 0.07
3.9Cu-NOC	15.0	3.9	0.59 ± 0.08
5.9Cu-NOC	21.2	5.9	0.49 ± 0.04

aberration corrected high-angle annular dark-field scanning transmission electron microscopy (AC-HAADF-STEM) images, which provide heavy Z-contrast. Bright isolated spots corresponding to Cu atoms are observed in Figs. 2(a)–2(d), demonstrating their uniform distribution on lamellar thin-layer nanosheets. The uniform distribution of Cu atoms was confirmed across multiple images. Approximately 200 atoms were considered for computational statistics to determine the average d_{site} between Cu atoms. These distances followed a normal distribution, which was accurately fitted using a nonlinear Gaussian's fitting function. The average d_{site} values are presented in Figs. 2(e)–2(h) and summarized in Table 1. For the sample with the lowest Cu loading (0.3Cu-NOC), the d_{site} was measured to be 1.62 ± 0.10 nm. As the Cu loading increased in the samples 2.0Cu-NOC, 3.9Cu-NOC, and 5.9Cu-NOC, the d_{site} values decreased to 0.68 ± 0.07, 0.59 ± 0.08, and 0.49 ± 0.04 nm, respectively. These results indicate that increasing the at.% of Cu leads to a reduction in d_{site} value, as shown in Fig. 2(i), which plots the correlation of Cu atomic contents with different d_{site} values.

X-ray photoelectron spectroscopy (XPS) was employed to analyze the chemical states and electronic environment of the dispersed Cu atoms. The Cu 2p spectra in Fig. 2(j) show binding energies in the range of 932.5–934.0 eV, which are characteristic of Cu^+ and Cu^{2+} oxidation states. Peak intensities increased proportionally with a higher Cu loading. No significant peaks were observed in the range of 940–945 eV, indicating the absence of CuO. The absence of CuO signals further supports the characteristic of SACs in our catalysts. Together, the HAADF-STEM and XPS results provide evidence for the successful synthesis of atomically dispersed Cu catalysts.

2.2 Catalytic performance

Figure 3(a) illustrates the catalytic performance of NOC, 0.3Cu-NOC, 2.0Cu-NOC, 3.9Cu-NOC, and 5.9Cu-NOC in the treatment of CIP over time. CIP concentration was detected by UV–visible (UV–vis) spectrophotometry at λ_{max} = 276 nm (Fig. S3 in the ESM), following a sequence of adsorption and degradation via PMS activation. The oxidant PMS alone exhibited negligible CIP degradation. Prior to PMS activation, an adsorption process was conducted for 60 min. Figure 3(b) shows the adsorptive removal of CIP by the *x*Cu-NOC catalysts. As the copper content increased from 0.3 at.% to 5.9 at.%, the adsorption capacity (Q_e) decreased from 7.80 to 0.93 mg/g. The correlation between Q_e and Cu density, as shown in inset of Fig. 3(b), can be expressed by the linear equation $y = -1.196x + 7.439$. The slope indicates that for every percent increase in Cu at.%, Q_e decreases by approximately 1.2 mg/g. Brunauer–Emmett–Teller (BET) analysis further supports this trend. As shown in Fig. S4 in the ESM, the specific surface area gradually decreases with increasing Cu loading, with values of 370, 353, 316, 313, and 302 m^2/g for NOC, 0.3Cu-NOC, 2.0Cu-NOC, 3.9Cu-NOC, and 5.9Cu-NOC, respectively. NOC exhibits a high adsorption capacity due to its porous structure and nitrogen doping, which introduce active sites for CIP adsorption. However, increasing the copper loading likely blocks some of these active sites, thereby reducing the overall adsorption capacity.

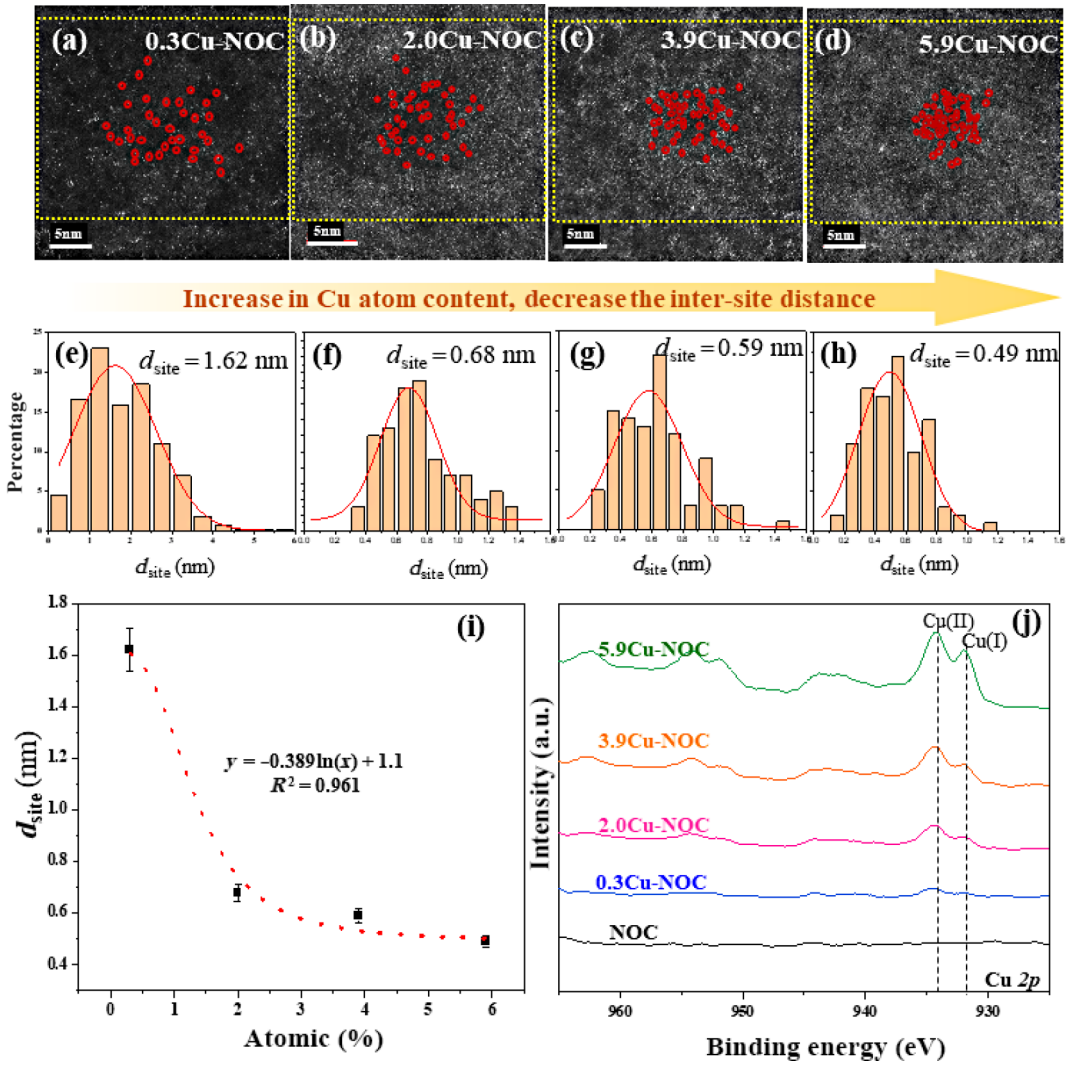

Figure 2 HAADF-STEM images (scale bars: 5 nm) and statistical distributions of the average d_{site} between adjacent Cu atoms for four samples with varying Cu loadings: ((a) and (e)) 0.3Cu-NOC, ((b) and (f)) 2.0Cu-NOC, ((c) and (g)) 3.9Cu-NOC, and ((d) and (h)) 5.9Cu-NOC. (i) Correlation of Cu atomic contents with different d_{site} values. (j) XPS profile C 2p spectra of *x*Cu-NOC with varying Cu loadings.

Figure 3(a) and Fig. S5(a) in the ESM compare the catalytic degradation of CIP over NOC and Cu-NOC catalysts via PMS activation. Among the tested samples, 5.9Cu-NOC achieves complete CIP degradation within 30 min with an apparent rate constant of 0.3242 min^{-1} (Fig. S5(b) in the ESM), whereas 0.3Cu-NOC, 2.0Cu-NOC, and 3.9Cu-NOC require up to 180 min to reach complete degradation. The superior catalytic activity of 5.9Cu-NOC is associated with its optimized Cu d_{site}, which is proposed to favor efficient PMS activation. This interpretation is supported by EPR results (Fig. 4). The time-dependent evolution of stronger 5,5-dimethyl-1-pyrroline N-oxide (DMPO)-radical adduct signals (Figs. 4(a) and 4(b)) and 2,2,6,6-tetramethylpiperidine (TEMP)-$^1O_2$ signals (Fig. 4(c)) indicates enhanced generation of both radical and non-radical reactive oxygen species on 5.9Cu-NOC. In contrast, Figs. 4(d)–4(f) show that catalysts with larger d_{site} such as 0.3Cu-NOC (1.62 nm) exhibit weaker EPR signals, particularly for DMPO-$\cdot O_2^-$, and lower catalytic activity. These observations are consistent with previous studies highlighting the critical role of atomic spacing in regulating catalytic activity through site synergy and reactant activation [33, 35].

To further elucidate the catalytic mechanism, we proposed the molecular geometry of 5.9Cu-NOC (Fig. 3(f)), based on the same synthesis method and chemical ratios reported by Jin et al. [28]. The structure features a Cu_1-N_3O_1 coordination environment, which is supported by the O 1s XPS spectra in Fig. 3(g), where the presence of Cu–O and C=O peaks is confirmed. The intensities of Cu–O peak at 530.7 eV gradually enhance with increasing the Cu density. Additionally, the XPS analysis of the atomic content in Table S1 in the ESM reveals that the ratio of N to O is maintained at approximately 3, suggesting that Cu SAC likely exist as a Cu_1-N_3O_1 moiety. This coordination environment has been demonstrated to effectively stabilize atomically dispersed Cu species with d_{site} of 0.49 nm.

2.3 Response surface methodology optimization

RSM was employed to investigate the influence of key factors on CIP degradation efficiency. A central composite design (CCD) was used to formulate the experimental design, optimizing CIP degradation by systematically adjusting reaction parameters. The CCD generated an experimental matrix of 27 runs (Table S2 in the ESM), incorporating four critical parameters: d_{site} (A), reaction time (B), catalyst dosage (C), and PMS concentration (D). The

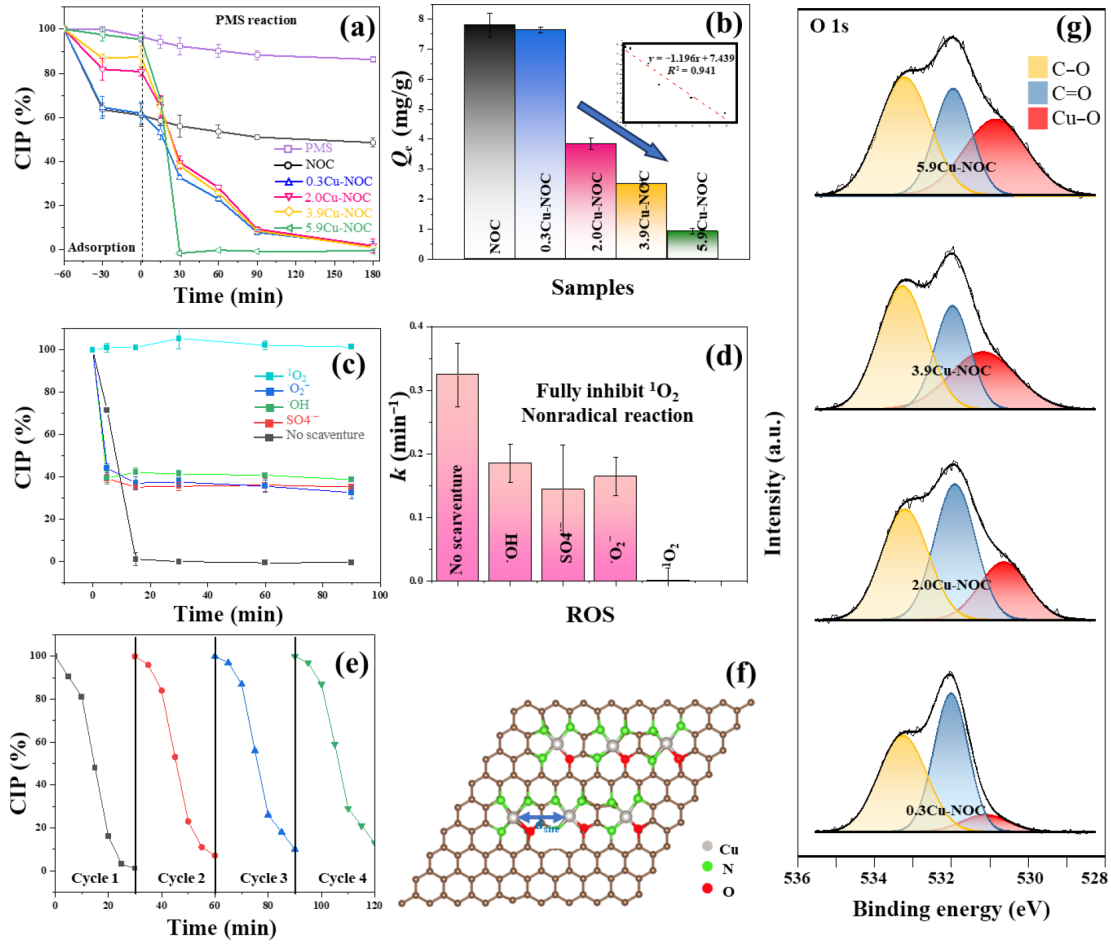

Figure 3 (a) The CIP degradation efficiency. (b) The adsorption efficiency. (c) The influence of different radical scavengers on the degradation of CIP. (d) Contribution of ROS quenching to the kinetic rate of CIP degradation. (e) Effectively reusable profiles of the 5.9Cu-NOC (experimental conditions: [5.9Cu-NOC] = 0.1 g/L, [PMS] = 0.5 mM, and [CIP] = 20 mg/L). (f) Proposed structures of 5.9Cu-NOC. (g) O 1s XPS spectra of *x*Cu-NOC samples with varying Cu loadings.

corresponding actual and predicted responses are presented in Fig. S6 in the ESM. The quadratic regression model for CIP degradation is expressed in Eq. (1)

$$\text{Degradation}(\%) = 69 + 15A + 6B + 39C + 13D + 3AB + 42AC + 4AD - BC - 3BD - 13A^2 + 21C^2 - 6D^2 \quad (1)$$

This equation captures the combined effects and interactions of the studied variables on CIP degradation efficiency. The analysis of variance (ANOVA) was conducted to assess the significance of the RSM model. The results (Table S3 in the ESM) indicate that the quadratic model with 14 predictors provides a statistically significant fit ($p < 0.001$), explaining a substantial proportion of the variance in the response variable. Additionally, the high coefficient of determination ($R^2 = 0.959$) shown in Fig. S6(a) in the ESM confirms a strong correlation between predicted and actual degradation values. The residuals plot (Figs. S6(b) and S6(c) in the ESM) further validates the model's reliability, with all residuals falling within ±2%, demonstrating its predictive accuracy. The three-dimensional (3D) and contour response surface plots in Fig. S7 in the ESM and the data presented in Table 2 demonstrate significant main effects for factors B ($p = 0.022$), C ($p = 0.004$), and D ($p = 0.001$), with factor D exerting the strongest influence ($F = 19.887$). Additionally, the interaction term AD ($p = 0.001$) was highly significant, revealing a synergistic effect between factors A and D. Although factor A alone is not significant ($p = 0.162$), its synergy with D drives reactivity, consistent with the findings of Wang et al., who reported that the optimal d_{site} in Cu/NG SAC maximizes peroxydisulfate (PDS) activation for BPA degradation [35]. The dominance of the AD term suggests that d_{site} is most effective in influencing PMS activation, ROS generation, and CIP degradation when considered along with PMS concentrations. Notably, the role of d_{site} does not rely solely on its abundance or the ratio of active sites. Its effectiveness is governed by geometric and electronic compatibility with PMS molecules. When the spatial and chemical optimal spatial arrangement between the active sites and the oxidant is optimal, the reaction efficiency can be substantially enhanced. This finding supports that the catalytic design should prioritize the optimal spatial arrangement of active site configurations with reactants over isolated parameter optimization.

2.4 Identification of ROS

2.4.1 Radical quenching experiments

5.9Cu-NOC was selected as the target catalyst for further investigation of reactive oxygen species using quenching experiments. The contributions of different ROS were evaluated using selective scavengers (Figs. 3(c) and 3(d)). When furfuryl alcohol (FFA), a specific $^1O_2$ quencher [37], was added, it reacted

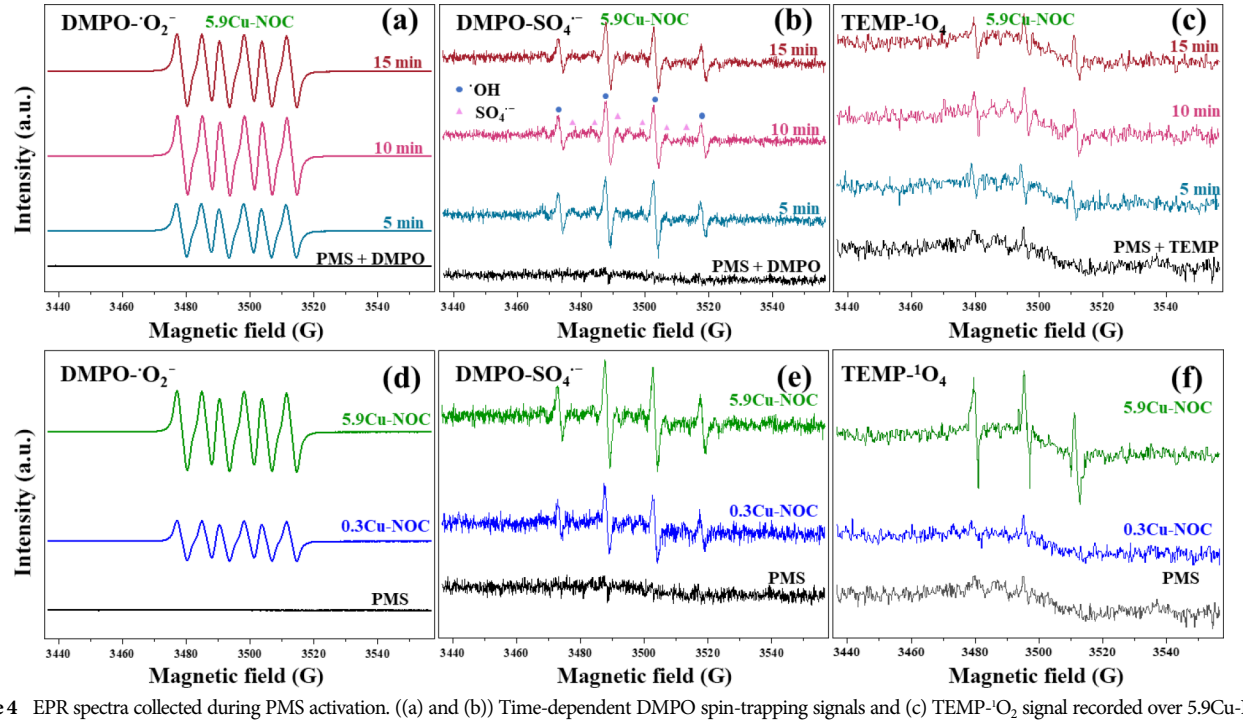

Figure 4 EPR spectra collected during PMS activation. ((a) and (b)) Time-dependent DMPO spin-trapping signals and (c) TEMP-$^1O_2$ signal recorded over 5.9Cu-NOC. ((d)–(f)) Comparison of DMPO and TEMP spin-trapping signals over 0.3Cu-NOC and 5.9Cu-NOC.

Table 2 Type I sum of squares analysis

Source	DF	Sum of squares	Mean squares	*F*	$P_r > F$	Sig. codes[a]
A	1.000	275.824	275.824	2.221	0.162	°
B	1.000	858.318	858.318	6.910	0.022	*
C	1.000	1530.254	1530.254	12.320	0.004	**
D	1.000	2470.129	2470.129	19.887	0.001	***
AA	1.000	278.160	278.160	2.240	0.160	°
AB	1.000	51.453	51.453	0.414	0.532	°
AC	1.000	19.181	19.181	0.154	0.701	°
AD	1.000	2444.052	2444.052	19.677	0.001	***
BB	1.000	18.135	18.135	0.146	0.709	°
BC	1.000	6.473	6.473	0.052	0.823	°
BD	1.000	138.489	138.489	1.115	0.312	°
CC	1.000	1727.705	1727.705	13.910	0.003	**
CD	1.000	3.450	3.450	0.028	0.870	°
DD	1.000	613.706	613.706	4.941	0.046	*

[a]Significance codes: 0 < *** < 0.001 < ** < 0.01 < * < 0.05 < ° < 0.1

with $^1O_2$ and prevented its interaction with CIP, almost completely inhibiting the degradation. This confirms that $^1O_2$ is the dominant and essential oxidant in the system. The addition of methanol (a scavenger for both $SO_4^{\cdot-}$ and ·OH [38]) significantly suppressed CIP degradation, with degradation terminating at approximately 65%, confirming the presence of $SO_4^{\cdot-}$ and indicating the involvement of radical pathways. In contrast, tert-butanol (a preferential ·OH scavenger [39, 40]) inhibited degradation by about 60%, indicating the contribution of ·OH. The addition of p-benzoquinone (an $\cdot O_2^-$ scavenger [26, 38, 41]) led to a noticeable inhibition, with degradation terminating around 68%. Collectively, these results indicate a mixed radical–non-radical mechanism, with $^1O_2$ serving as the rate-limiting species. As shown in Fig. 3(d), the kinetic analysis further confirms that radical pathways contribute marginally to CIP degradation, with rate constants of 0.1438, 0.1642, and 0.1854 min^{-1} for $SO_4^{\cdot-}$, $\cdot O_2^-$, and ·OH, respectively. These findings align with prior studies on SACs. Yang et al. [30] demonstrated that Cu SACs with unsaturated B,O-coordination selectively generate $^1O_2$ via PMS activation, achieving a CIP degradation rate of 0.2250 min^{-1} and a $^1O_2$ selectivity near 100%, and Li et al. [42] precisely regulated the spin states of Fe^{III} by N_2,O_2,Cl-coordination for the selective generation of $^1O_2$ in PMS-AOPs up to 86.4%.

2.4.2 *EPR spectroscopy for ROS detection*

EPR spin-trapping experiments were performed to directly identify

the generated ROS. Using DMPO as a spin trap, the signal characteristics of DMPO-·O_2^-, DMPO-$SO_4^{\cdot-}$, and DMPO-·OH adducts were detected over 5.9Cu-NOC (Figs. 4(a) and 4(b)), confirming the generation of multiple radical species. For instance, the six-line signal with a 1:1:1:1:1:1 intensity ratio, characteristic of DMPO-·O_2^-, and the 1:2:2:1 quartet signal of DMPO-$SO_4^{\cdot-}$ were clearly observed. In parallel, TEMP was used to trap $^1O_2$, yielding a characteristic 1:1:1 triplet signal of 2,2,6,6-tetramethylpiperidin-1-oxyl (TEMPO) (Fig. 4(c)), confirming the $^1O_2$ generation. The time-dependent increase in all EPR signals indicated sustained ROS production during PMS activation. For comparison, the catalyst with the longest d_{site} (0.3Cu-NOC, 1.62 nm) showed markedly weaker EPR signals (Figs. 4(d)–4(f)), especially for DMPO-·O_2^- and TEMPO, consistent with its inferior catalytic performance.

2.4.3 *Potassium iodide (KI)-based PMS consumption analysis and pollutant-involved redox participation*

To further examine the redox processes involved in PMS activation, a KI–based colorimetric method was employed to monitor PMS consumption. PMS can oxidize I^- to I_2, which subsequently reacts with excess iodide to form triiodide I_3^-, exhibiting a characteristic UV–vis absorption signal. The relevant reactions are expressed as follows

$$HSO_5^- + 2I^- + H^+ \rightarrow HSO_4^- + I_2 + H_2O \quad (2)$$

$$I_2 + I^- \rightleftharpoons I_3^- \quad (3)$$

This iodometric reaction reflects the oxidizing capacity of PMS and has been widely applied to quantify residual persulfate species in AOP [43]. Notably, the oxidation of iodide is inherently a redox process involving electron transfer [44].

As shown in Fig. S8 in the ESM, the KI-based iodometric analysis, supported by the calibration curve in Fig. S9 in the ESM, reveals a clear dependence of PMS consumption on Cu loading during catalytic activation. In the absence of organic substrates, the residual PMS signal decreases progressively with increasing Cu content, following the order of PMS alone > 0.3Cu-NOC > 2.0Cu-NOC > 3.9Cu-NOC > 5.9Cu-NOC. This trend indicates that a higher density of Cu single-atom sites accelerates the PMS consumption, reflecting enhanced PMS activation efficiency.

Notably, the introduction of CIP into the 5.9Cu-NOC/PMS/KI system results in a markedly faster decline in the residual PMS signal, yielding the lowest PMS level within 30 min. This substrate-dependent acceleration demonstrates that organic molecules actively participate in the redox processes associated with PMS activation rather than acting solely as oxidation targets. The enhanced PMS decay in the presence of CIP suggests that the Cu single-atom catalyst facilitates redox interactions between PMS and organic substrates, thereby promoting the oxidant consumption.

Overall, these results indicate that PMS activation is jointly governed by Cu d_{site} and pollutant-assisted redox participation. The observed enhancement of PMS consumption in the presence of organic substrates is consistent with redox-assisted persulfate activation mechanisms reported in previous studies [45], where the surface-mediated redox processes favor non-radical oxidation pathways.

2.4.4 *Solvent isotope effect (D_2O vs. H_2O)*

To elucidate the role of $^1O_2$ in the non-radical PMS activation pathway, degradation kinetics were compared in H_2O and D_2O. Because the lifetime of $^1O_2$ in D_2O (20–32 μs) is more than ten times longer than that in H_2O (~ 2 μs) [46], a significant rate enhancement in D_2O is typically expected for $^1O_2$-dominated reactions [45]. As shown in Fig. S10 in the ESM, the degradation rate in D_2O is only marginally higher than that in H_2O, confirming the generation of $^1O_2$ in the 5.9Cu-NOC/PMS system while also suggesting that $^1O_2$ reacts in a surface-confined manner rather than diffusing into the bulk solution.

2.5 The catalysis mechanism

Figure 5 illustrates the proposed dual-pathway mechanism for CIP degradation over the 5.9Cu-NOC catalyst, integrating the adsorption, PMS activation, and pollutant-dependent redox participation. The catalyst, featuring an optimized Cu–Cu d_{sites} of

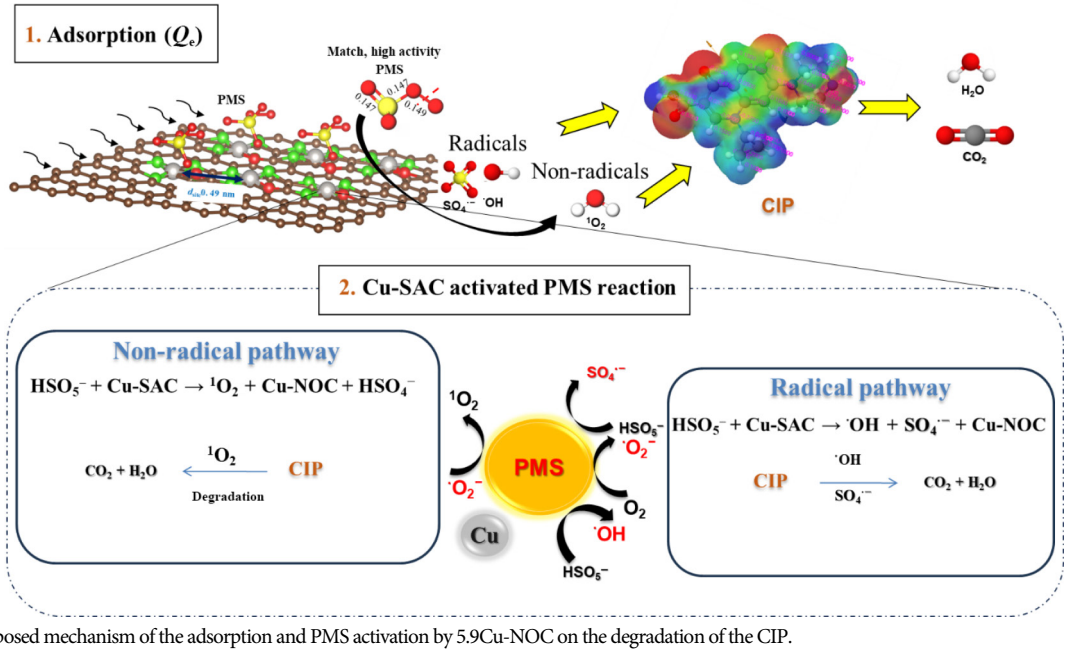

Figure 5 A proposed mechanism of the adsorption and PMS activation by 5.9Cu-NOC on the degradation of the CIP.

0.49 nm, facilitates PMS bridging between adjacent Cu sites. This geometry-matched configuration stabilizes PMS adsorption and lowers the activation barrier for O–O bond cleavage [35], thereby promoting both radical and non-radical activation pathways. Similar interfacial regulation of PMS activation has been reported in recent studies, where electronically coupled metal sites enhance oxidant adsorption and enable surface-mediated redox processes [47]. On this basis, the PMS activation in the present system proceeds through two parallel reaction routes.

The first route involves the $^1O_2$ generation via a non-radical pathway. PMS interacts with closely spaced Cu sites, favoring the formation of surface-bound reactive oxygen intermediates that subsequently evolve into $^1O_2$. This pathway is supported by the complete inhibition in the presence of FFA, direct detection of TEMP-$^1O_2$ adducts by EPR spectroscopy, and the enhanced degradation rate observed in D_2O, collectively confirming that $^1O_2$ is the dominant reactive species and primarily reacts at or near the catalyst surface. This surface-confined non-radical oxidation behavior is consistent with prior reports demonstrating that interfacial electronic modulation suppresses free-radical diffusion while promoting selective non-radical oxidation [47].

The second route comprises radical-assisted and redox-associated pathways. Concurrent PMS activation generates radical species, including $SO_4^{\bullet-}$, ·OH, and $\cdot O_2^-$, as evidenced by EPR signals and partial inhibition by methanol, tert-butanol, and p-benzoquinone. In addition, CIP itself participates in PMS activation through pollutant-involved redox interactions. The pronounced enhancement of PMS consumption observed by the KI assay in the presence of CIP indicates that organic substrates promote the oxidant decay via redox participation. Given that the PMS activation inherently involves electron-accepting steps [44], and that KI-based iodometric methods reliably reflect the persulfate consumption in redox-driven systems [43], these results suggest that the Cu single-atom sites mediate electron donation from CIP to PMS, contributing an additional oxidation channel alongside the radical pathway. Similar pollutant-assisted redox participation during PMS activation, where organic molecules act as active electron donors rather than passive targets, has been reported in related catalytic systems [46].

The optimized Cu–Cu spacing of 0.49 nm is therefore critical for this dual functionality: It enables efficient PMS bridging for non-radical $^1O_2$ generation while simultaneously facilitating CIP adsorption and redox participation between adjacent Cu sites. This geometric and electronic synergy accounts for the superior catalytic performance of 5.9Cu-NOC, which achieves complete CIP degradation within 30 min, whereas catalysts with larger inter-site distances (0.57–1.62 nm) require substantially longer reaction time.

Although the disappearance of the CIP absorbance peak at 276 nm confirms effective degradation of the parent compound, this study did not directly identify transformation products or assess their toxicity. Previous PMS-based oxidation studies report that CIP undergoes stepwise oxidation processes, including hydroxylation, defluorination, piperazine-ring opening, and cleavage of the quinolone core, yielding smaller organic fragments and inorganic species [48]. Although these pathways suggest progressive molecular breakdown, comprehensive product identification and toxicity evaluation remain necessary for a complete environmental risk assessment and should be addressed in future studies. This work demonstrates a dual-pathway mechanism for CIP degradation over the 5.9Cu-NOC catalyst, integrating adsorption, PMS activation, and pollutant-dependent electron transfer.

2.6 Recyclability

The recyclability of the 5.9Cu-NOC catalyst was evaluated through consecutive CIP degradation cycles under identical reaction conditions. As shown in Fig. 3(e), each catalytic cycle was conducted for a fixed reaction time of 30 min. The CIP removal efficiency gradually decreased over repeated cycles, reaching approximately 87% after four cycles. This result indicates that the catalyst maintains reasonable cyclic performance, although a gradual decline in activity is observed rather than complete retention of the initial performance.

In addition, the Cu leaching was evaluated by ICP analysis (Table S4 in the ESM). The Cu content of fresh 5.9Cu-NOC is 21.22 wt.%, while that of the used catalyst after PMS activation decreases slightly to 20.86 wt.%, corresponding to a Cu loss of less than 2%. Although a small amount of Cu is lost during recycling, this minor leaching may partially reduce the number of Cu active sites and weaken their cooperative effect in PMS activation. Such metal leaching behavior is a common challenge in Fenton-like systems, yet recent studies have shown that constructing robust heterointerfaces can significantly suppress metal dissolution and enhance catalyst stability [49]. In addition, the strongly oxidative reaction environment may lead to surface fouling or slight changes in the local coordination environment of active sites. As a result, the gradual decline in performance is likely caused by a combination of Cu loss and surface or structural changes of the active sites. Overall, the above results indicated that 5.9Cu-NOC/PMS system had relatively good stability and recoverability.

2.7 Potential use capacity in complex water

To evaluate the robustness of the Cu-SAC/PMS system under non-ideal laboratory conditions, the effects of common inorganic ions, including Cl^-, HCO_3^-, and Ca^{2+}, on CIP degradation were examined (Fig. 6). As shown in Fig. 6(a), the presence of Cl^- and Ca^{2+} at 20 mM causes only a modest delay in CIP degradation compared with the blank system, while efficient removal is still achieved over the reaction period. In contrast, HCO_3^- at the same concentration results in a pronounced suppression of CIP degradation, indicating stronger interference with PMS activation. Further concentration-dependent experiments (Figs. 6(b)–6(d)) show that increasing Cl^- concentration leads to only minor changes in degradation behavior, whereas higher levels of HCO_3^- progressively inhibit CIP degradation. The presence of Ca^{2+} induces a moderate retardation effect, particularly at higher concentrations, which may be associated with increased ionic strength and surface interactions rather than direct radical scavenging. Overall, although degradation is influenced by ion type and concentration, substantial CIP removal is still observed under most tested conditions, demonstrating that the Cu-SAC/PMS system maintains catalytic functionality in the presence of common inorganic ions.

3 Conclusions

In summary, high-loading Cu single-atom catalysts with systematically tuned Cu–Cu d_{site} were successfully synthesized and evaluated for PMS activation toward CIP degradation. Comprehensive structural characterization confirmed atomic dispersion of Cu, with d_{site} values ranging from 1.62 to 0.49 nm as

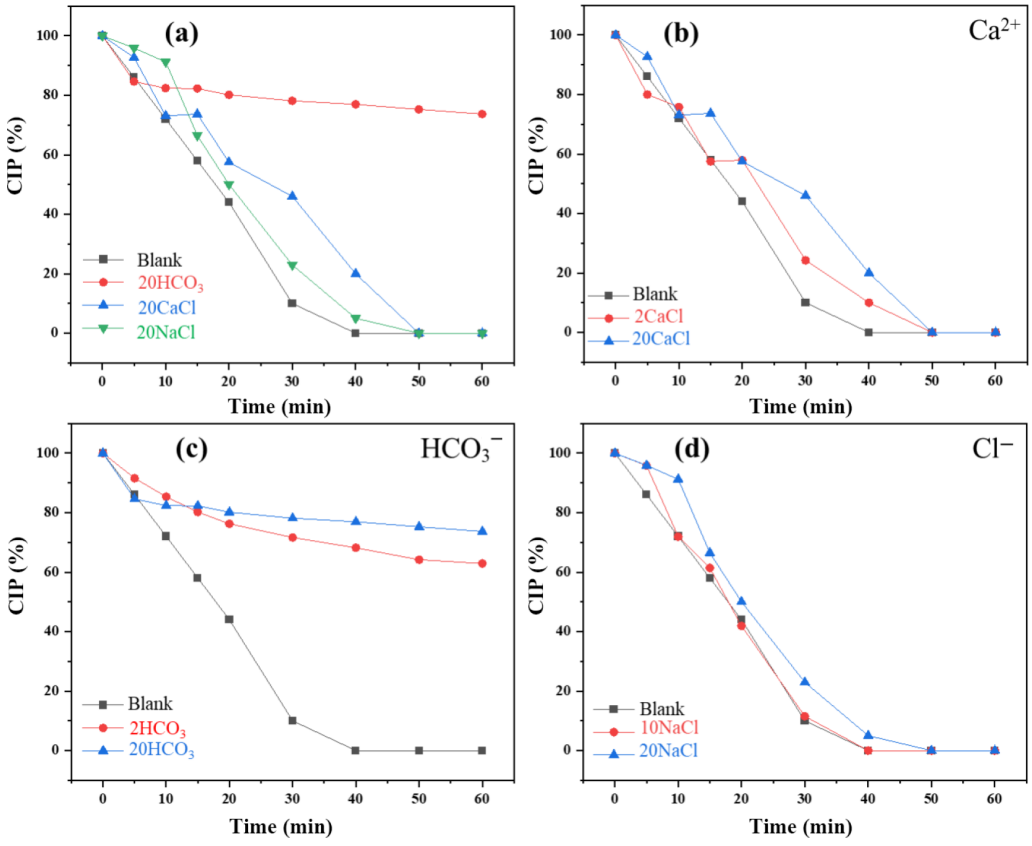

Figure 6 (a) Effect of ionic impurity (HCO_3^-, Ca^{2+}, and Cl^-) at a fixed concentration of 20 mM on CIP degradation in the Cu-SAC/PMS system. ((b)–(d)) Influence of Ca^{2+}, HCO_3^-, and Cl^- at different concentrations on CIP degradation (experimental conditions: [5.9Cu-NOC] = 0.1 g/L, [PMS] = 0.5 Mm, and [CIP] = 20 mg/L).

the Cu loading increased. The 5.9Cu-NOC catalyst, with an optimal d_{site} of 0.49 nm, exhibited superior catalytic performance, achieving complete CIP degradation within 30 min with an apparent rate constant of 0.3242 min^{-1}, significantly outperforming catalysts with larger inter-site spacings. The enhanced activity is attributed to the geometry-matched spatial arrangement of Cu sites, which facilitates efficient PMS bridging and activation. Through a combination of quenching experiments, EPR spectroscopy, KI-based PMS consumption analysis, and D_2O/H_2O solvent isotope effect, the reaction mechanism was elucidated as a dual-pathway process: (1) a dominant surface-confined singlet $^1O_2$ pathway, supported by complete FFA inhibition and TEMPO detection, and (2) auxiliary radical pathways involving $SO_4^{\bullet-}$, ·OH, and $\cdot O_2^-$, alongside with CIP pollutant-involved redox interactions. The minimal solvent isotope effect further confirmed that $^1O_2$ reacts at the catalyst surface rather than in the bulk solution. This work provides a rational geometric principle for the development of high-performance SACs for environmental remediation and highlights the importance of dual-pathway activation in pollutant degradation.

Electronic Supplementary Material: Supplementary material (experimental section, UV–vis spectra, SEM and TEM images, RSM quadratic regression model and surface contour plot, and XPS results) is available in the online version of this article at https://doi.org/10.26599/NR.2026.94908537.

Data availability

All data needed to support the conclusions in the paper are presented in the manuscript and the Electronic Supplementary Material. Additional data related to this paper may be requested from the corresponding author upon request.

Acknowledgements

We thank the National Natural Science Foundation of China (Nos. 22272181 and 52321006). We thank Dr. Jin Hongqiang for his assistance with HAADF-STEM characterization. P. M. acknowledges support from the Royal Thai Government.

Declaration of competing interest

All the contributing authors report no conflict of interests in this work.

Author contribution statement

P. M.: Conceptualization, methodology, investigation, formal analysis, data curation, writing – original draft. Y. M. Y.: Investigation, characterization. K. X. Z.: Methodology. R. R. X.: Characterization. C. Y. C.: Conceptualization, data curation, supervision, writing – review & editing. W. G. S.: Conceptualization, resources, supervision, writing – review & editing. All the authors have approved the final manuscript.

Use of AI statement

None.

References

[1] Girardi, C.; Greve, J.; Lamshöft, M.; Fetzer, I.; Miltner, A.; Schäffer, A.; Kästner, M. Biodegradation of ciprofloxacin in water and soil and its effects on the microbial communities. *J. Hazard. Mater.* **2011**, *198*, 22–30.

[2] Laib, I.; Bouafia, A.; Laouini, S. E.; Abdullah, M. M. S.; Al-Lohedan, H. A.; AlEssa, E. M.; Ahmed Abdullah, J. A. Ciprofloxacin-loaded copper oxide nanoparticles: Cutting-edge multifunctional nano-therapeutics with superior antidiabetic, antioxidant, anti-inflammatory, and antibacterial potency against drug-resistant pathogens. *J. Cryst. Growth* **2025**, *653*, 128074.

[3] Jalali, M. A.; Mousavi, S. M.; Setoodehkhah, M. Efficient removal of ciprofloxacin from pharmaceutical wastewater using advanced oxidation processes on doped perovskite $La_{0.5}A_{0.5}CoO_3$ (A = Sr, Ba and Ce) nanocatalysts. *Appl. Catal. O: Open.* **2025**, *199*, 207024.

[4] Kini, V.; C S, S.; Mondal, D.; Sundarabal, N.; Nag, P.; Sadani, K. Recent advances in electrochemical sensing and remediation technologies for ciprofloxacin. *Environ. Sci. Pollut. Res.* **2025**, *32*, 2210–2237.

[5] Kumar, S.; Dey, P.; Pathak, A. K.; Wadawale, A.; Maurya, D. K.; Natu, K.; Bose, K.; Goswami, D. Structure-activity relationship of ciprofloxacin towards S-spike protein of SARS-CoV-2: Synthesis and *in-silico* evaluation. *J. Chem. Inf. Model.* **2025**, *65*, 825–844.

[6] Han, S.; Wang, Z. L.; Huang, H. M.; Wang, T.; Zhou, Z. L.; Bai, Y.; Du, P.; Li, X. Q. Estimating antibiotics use in major cities in China through wastewater-based epidemiology. *Sci. Total Environ.* **2022**, *826*, 154116.

[7] Ma, C. Y.; Guo, Y. J.; Zhang, D. F.; Wang, Y. H.; Li, N. N.; Ma, D.; Ji, Q.; Xu, Z. H. Metal-nitrogen-carbon catalysts for peroxymonosulfate activation to degrade aquatic organic contaminants: Rational design, size-effect description, applications and mechanisms. *Chem. Eng. J.* **2023**, *454*, 140216.

[8] Ali, Q.; Zainab, R.; Badshah, M.; Sarwar, W.; Khan, S.; Mustafa, G.; Ibrahim, T.; Ahmed, S. Prospecting the biodegradation of ciprofloxacin by *Stutzerimonas stutzeri* R2 and *Exiguobacterium indicum* strain R4 isolated from pharmaceutical wastewater. *H2Open J.* **2024**, *7*, 149–162.

[9] Wang, Y.; Shen, C. C.; Zhang, M. M.; Zhang, B. T.; Yu, Y. G. The electrochemical degradation of ciprofloxacin using a SnO_2-Sb/Ti anode: Influencing factors, reaction pathways and energy demand. *Chem. Eng. J.* **2016**, *296*, 79–89.

[10] Manpetch, P.; Singhapong, W.; Jaroenworaluck, A. A comparative study of TiO_2 nanoparticles and Cu(II)/TiO_2 nanocomposites on photodegradation of cinnamic acid (CA) under natural sunlight and artificial UV light. *J. Dispersion Sci. Technol.* **2023**, *44*, 2267–2279.

[11] Asgari, E.; Sheikhmohammadi, A.; Nourmoradi, H.; Nazari, S.; Aghanaghad, M. Degradation of ciprofloxacin by photocatalytic ozonation process under irradiation with UVA: Comparative study, performance and mechanism. *Process Saf. Environ. Prot.* **2021**, *147*, 356–366.

[12] Pignatello, J. J.; Oliveros, E.; MacKay, A. Advanced oxidation processes for organic contaminant destruction based on the fenton reaction and related chemistry. *Crit. Rev. Environ. Sci. Technol.* **2006**, *36*, 1–84.

[13] DeWitte, B.; Dewulf, J.; Demeestere, K.; Van De Vyvere, V.; De Wispelaere, P.; Van Langenhove, H. Ozonation of ciprofloxacin in water: HRMS identification of reaction products and pathways. *Environ. Sci. Technol.* **2008**, *42*, 4889–4895.

[14] Hou, J. F.; He, X. D.; Zhang, S. Q.; Yu, J. L.; Feng, M. B.; Li, X. D. Recent advances in cobalt-activated sulfate radical-based advanced oxidation processes for water remediation: A review. *Sci. Total Environ.* **2021**, *770*, 145311.

[15] Xu, N.; Liu, K. X.; Liu, Q.; Wang, Q.; Zhu, A. Z.; Fan, L. Peroxymonosulfate enhanced photocatalytic degradation of organic dye by metal-free TpTt-COF under visible light irradiation. *Sci. Rep.* **2024**, *14*, 8183.

[16] Li, D. H.; Zhang, S. X.; Li, S. N.; Tang, J. C.; Hua, T.; Li, F. X. Mechanism of the application of single-atom catalyst-activated PMS/PDS to the degradation of organic pollutants in water environment: A review. *J. Cleaner Prod.* **2023**, *397*, 136468.

[17] Wang, J.; Bi, S. M.; Zhang, Y.; Shen, Y.; Lu, L.; Duan, X. G.; Tan, X. Y.; Wang, S. B. Single-atom coordination-dependent catalysis for peroxymonosulfate-mediated water purification. *Curr. Opin. Chem. Eng.* **2023**, *41*, 100931.

[18] Kang, D. W.; Kim, J. H.; Lim, J. H.; Kim, Y.; Kang, M.; Shin, J.; Son, S.; Yun, H.; Kim, H.; Park, S. et al. Promoted type I and II ROS generation by a covalent organic framework through sonosensitization and PMS activation. *ACS Catal.* **2022**, *12*, 9621–9628.

[19] Kumari, M.; Pulimi, M. Sulfate radical-based degradation of organic pollutants: A review on application of metal-organic frameworks as catalysts. *ACS Omega* **2023**, *8*, 34262–34280.

[20] Fu, J. Y.; Feng, L.; Liu, Y. Z.; Zhang, L. Q.; Li, S. Electrochemical activation of peroxymonosulfate (PMS) by carbon cloth anode for sulfamethoxazole degradation. *Chemosphere* **2022**, *287*, 132094.

[21] Xu, Y. D.; Guo, M. X.; Ge, C. J.; Zhang, P.; Xu, W.; Zhang, L. L.; Zhou, S. H.; Liao, J. J. Cu single atoms/O doping g-C_3N_4 mediated photocatalytic activation of peroxymonosulfate for ultrafast carbamazepine removal via high $^1O_2$ yield. *Appl. Surf. Sci.* **2023**, *640*, 158290.

[22] Yang, P. Z.; Long, Y. H.; Huang, W. L.; Liu, D. F. Single-atom copper embedded in two-dimensional MXene toward peroxymonosulfate activation to generate singlet oxygen with nearly 100% selectivity for enhanced Fenton-like reactions. *Appl. Catal. B: Environ.* **2023**, *324*, 122245.

[23] Lu, Z. C.; Zhang, P.; Hu, C.; Li, F. Insights into singlet oxygen generation and electron-transfer process induced by a single-atom Cu catalyst with saturated Cu–N_4 sites. *iScience* **2022**, *25*, 104930.

[24] Cheng, J. J.; Tu, X. M.; Wu, P. X.; Zhou, R. T.; Luo, S. H.; Zhang, L.; Zou, J. P.; Li, Y. H.; Johnson, H. M.; Zhang, Q. Directing the persulfate activation reaction pathway by control of Fe-N_x/C single-atom catalyst coordination. *Chem. Eng. J.* **2024**, *481*, 148603.

[25] Hu, J. Q.; Tian, J. L.; Yang, Y.; Li, S. S.; Lu, J. F. Enhanced antibiotic degradation via photo-assisted peroxymonosulfate over graphitic carbon nitride nanosheets/$CuBi_2O_4$: Highly efficiency of oxygen activation and interfacial charge transfer. *J. Colloid Interface Sci.* **2024**, *661*, 68–82.

[26] Bai, W. H.; Lu, H. Z.; Liu, Y.; Yuan, X.; Ai, Y. J.; Wang, L. D.; Chen, Z. Crystallinity regulation-induced organic degradation on ultra-thin 2D Co_3O_4/SiO_2 nanosheets: The critical trigger of oxygen vacancies. *Environ. Sci.: Nano* **2024**, *11*, 2507–2520.

[27] Hao, L. P.; Guo, C.; Hu, Z. Y.; Guo, R.; Liu, X. W.; Liu, C. M.; Tian, Y. Single-atom catalysts based on Fenton-like/peroxymonosulfate system for water purification: Design and synthesis principle, performance regulation and catalytic mechanism. *Nanoscale* **2022**, *14*, 13861–13889.

[28] Jin, H. Q.; Cui, P. X.; Cao, C. Y.; Yu, X. H.; Zhao, R. Q.; Ma, D.; Song, W. G. Understanding the density-dependent activity of Cu single-atom catalyst in the benzene hydroxylation reaction. *ACS Catal.* **2023**, *13*, 1316–1325.

[29] Cao, C. Y.; Song, W. G. Single-atom catalysts for thermal heterogeneous catalysis in liquid: Recent progress and future perspective. *ACS Mater. Lett.* **2020**, *2*, 1653–1661.

[30] Yang, P. Z.; Cao, Z. H.; Long, Y. H.; Liu, D. F.; Huang, W. L.; Zhan, S. H.; Li, M. Regulating the local electronic structure of copper single atoms with unsaturated B, O-coordination for selective $^1O_2$ generation. *ACS Catal.* **2023**, *13*, 12414–12424.

[31] Wang, X. X.; Zhang, C. Y.; Li, D. H.; Sun, Y. Y.; Ren, J.; Sun, J.;

Yang, D. J. Theoretical study of local S coordination environment on Fe single atoms for peroxymonosulfate-based advanced oxidation processes. *J. Hazard. Mater.* **2023**, *454*, 131469.
[32] Huang, B. K.; Ren, X. Y.; Zhao, J.; Wu, Z. L.; Wang, X. H.; Song, X. Y.; Li, X. N.; Liu, B.; Xiong, Z. K.; Lai, B. Modulating electronic structure engineering of atomically dispersed cobalt catalyst in fenton-like reaction for efficient degradation of organic pollutants. *Environ. Sci. Technol.* **2023**, *57*, 14071–14081.
[33] Zhang, S. Q.; Lu, Z. C.; Hu, C.; Li, F. Understanding the distance effect of the single-atom active sites in Fenton-like reactions for efficient water remediation. *Adv. Sci.* **2024**, *11*, 2307151.
[34] Jin, Z. Y.; Li, P. P.; Meng, Y.; Fang, Z. W.; Xiao, D.; Yu, G. H. Understanding the inter-site distance effect in single-atom catalysts for oxygen electroreduction. *Nat. Catal.* **2021**, *4*, 615–622.
[35] Wang, B. Q.; Cheng, C.; Jin, M. M.; He, J.; Zhang, H.; Ren, W.; Li, J.; Wang, D. S.; Li, Y. D. A site distance effect induced by reactant molecule matchup in single-atom catalysts for Fenton-like reactions. *Angew. Chem., Int. Ed.* **2022**, *61*, e202207268.
[36] Jing, T. Y.; Li, T. T.; Rao, D. W.; Wang, M. Y.; Zuo, Y. P. Defining the loading of single-atom catalysts: Weight fraction or atomic fraction. *Mater. Today Energy* **2023**, *31*, 101197.
[37] Zhou, X. Q.; Wei, X. F.; Lu, W. W.; Wang, H.; Liu, J. H.; Zhang, R. C.; Wang, H. B.; Wang, J. Multi- dimensional induction and analysis of singlet oxygen oxidation in persulfate-based catalytic oxidation systems. *Sep. Purif. Technol.* **2024**, *332*, 125811.
[38] Qi, C. D.; Liu, X. T.; Ma, J.; Lin, C. Y.; Li, X. W.; Zhang, H. J. Activation of peroxymonosulfate by base: Implications for the degradation of organic pollutants. *Chemosphere* **2016**, *151*, 280–288.
[39] Ma, T. T.; Guo, M. Z.; Cao, Y. Q.; Zhong, W. W.; Ding, C. C.; Ye, H. M.; Chen, L. Y.; Xu, H.; Fang, Z.; He, W. Switch PMS activation pathway from free radical to non-radical by introducing hexagonal boron nitride in supported $CoFe_2O_4$: The role of lattice oxygen and PMS adsorption. *J. Environ. Chem. Eng.* **2024**, *12*, 114823.
[40] Anipsitakis, G. P.; Dionysiou, D. D. Degradation of organic contaminants in water with sulfate radicals generated by the conjunction of peroxymonosulfate with cobalt. *Environ. Sci. Technol.* **2003**, *37*, 4790–4797.
[41] Cai, L. M.; Yao, Q.; Du, X. D.; Tao, X. Q.; Zou, M. Y.; Zhou, J. M.; Dang, Z.; Lu, G. N. Identification of superoxide contribution through the quenching method and model system. *ACS ES&T Eng.* **2024**, *4*, 2145–2154.
[42] Li, R. P.; Sun, W.; Yang, W. C.; Yuan, L. Z.; Wang, A. Q.; Huang, H. M.; Wong, J. W. C. Tailoring Fe^{III} spin states with N_2,O_2,Cl-coordination for highly selective peroxymonosulfate conversion to singlet oxygen. *Appl. Catal. B: Environ. Energy* **2025**, *378*, 125573.
[43] Liang, C. J.; Huang, C. F.; Mohanty, N.; Kurakalva, R. M. A rapid spectrophotometric determination of persulfate anion in ISCO. *Chemosphere* **2008**, *73*, 1540–1543.
[44] Zhu, Y. H.; Cui, Y. F.; Yang, H. Y. Revolution of iodine electrochemistry: From I^-/I_2 to I^-/I^{5+}. *Matter* **2024**, *7*, 2769–2770.
[45] Yun, E. T.; Lee, J. H.; Kim, J.; Park, H. D.; Lee, J. Identifying the nonradical mechanism in the peroxymonosulfate activation process: Singlet oxygenation versus mediated electron transfer. *Environ. Sci. Technol.* **2018**, *52*, 7032–7042.
[46] Wang, Y. Z.; Pan, Y.; Zhang, X. S.; Huang, X. Y.; Li, T.; Liu, S.; Tang, S. Q.; Sun, Y. Y.; Shao, B. B.; Liu, Z. F. Defect engineering boosting PMS activation activity on cobalt polyphthalocyanine: Promoting Co(IV)=O formation and enhancing $^1O_2$ selectivity. *Sep. Purif. Technol.* **2025**, *357*, 130085.
[47] Pan, Y.; Zhang, X. S.; Huang, X. Y.; Li, T.; Wu, T.; Shao, B. B.; Liu, S.; Wang, Y. Z.; Tang, S. Q.; Liu, Y. et al. Optimized the e occupancy of Co active site through 4f-2p-3d gradient orbital coupling for efficient Fenton-like catalysis. *Appl. Catal. B: Environ. Energy* **2025**, *375*, 125420.
[48] Caballero, A.; Perez-Sanchez, E.; Serrano-Lázaro, A.; Bizarro, M.; Martínez, A. Chemical characteristics of ciprofloxacin and its degradation products: On the road to understanding its potential hazards. *ACS Omega* **2025**, *10*, 58656–58670.
[49] Zhang, X. S.; Pan, Y.; Wang, Y. Z.; Wu, T.; Shao, B. B.; He, Q. Y.; Zhou, L. F.; Li, T.; Liu, S.; Huang, X. Y. et al. MOF derived $MnFeO_x$ supported on carbon cloth as electrochemical anode for peroxymonosulfate electro-activation and persistent organic pollutants degradation. *Chem. Eng. J.* **2024**, *481*, 148646.